Non-isothermal cold start of polymer electrolyte fuel cells

Fangming Jiang, Weifeng Fang, Chao-Yang Wang *

Department of Mechanical and Nuclear Engineering, and Electrochemical Engine Center (ECEC),
The Pennsylvania State University, University Park, PA 16802, USA

Abstract

A multiphase, three-dimensional model has been developed to describe non-isothermal cold start of a polymer electrolyte fuel cell (PEFC) and to delineate intricate interactions between ice formation and heat generation during cold start. The effect of rising cell temperature is numerically explored by comparing a non-isothermal cold start with an isothermal one. It is found that more water is transported into the membrane and less ice formation occurs in the cathode catalyst layer (CL) in the presence of rising cell temperature. In addition, the more hydrated membrane and the rising cell temperature greatly lower the membrane resistance, thus giving rise to higher cell voltage. A lumped thermal analysis significantly over-estimates the overall thermal requirement of self-startup as a cell requires only a portion of its active area to reach the freezing point and be ice-free and operable. It is also found that pre-startup conditions have significant influence on cold start. Procedures to minimize residual water inside the cell prior to cold start, such as gas purge, are critically important. Finally, non-isothermal cold start becomes much easier from higher ambient temperatures.

© 2007 Elsevier Ltd. All rights reserved.

Keywords: Polymer electrolyte fuel cell; Cold start; Modeling; Non-isothermal; Ice formation

1. Introduction

Quick startup of a polymer electrolyte fuel cell (PEFC) engine in a sub-freezing environment, referred to as "cold start", remains a significant challenge for automotive application. Recent experimental and theoretical studies [1–10] have revealed the fundamental principles underlying PEFC cold start; that is, water is removed from the cathode catalyst layer (CL) via absorption into the ionomeric membrane and via vapor-phase transport and subsequent desublimation in the gas diffusion layer (GDL)/channels. This is followed by ice formation in the CL. Consequently, key factors were identified, including the operating parameters, such as startup current density, ambient temperature and purge conditions prior to cell cool-down and freezing, as well as materials parameters of the membrane and CL [6,8,10].

The research in Refs. [3–9] also proposed a fundamental methodology based on isothermal cold start at a fixed cell temperature (below freezing). These isothermal studies, conducted

over a range of temperatures, established the needed physics to build an engineering model for forecasting practical cold-start processes involving rising cell temperature. Based on the dependence of cold-start characteristics on cell temperature as derived from the isothermal studies, the present work aims to develop a model of non-isothermal cold start for PEFCs possessing any thermal mass and operated under realistic automotive conditions. The present model is an extension of the multiphase model of Mao et al. [7], with focus on the interactions of water transport with heat transport and hence the rising cell temperature effect in non-isothermal cold start. Besides the exploration of tightly coupled water and heat transport involved in non-isothermal cold start, the present model can be employed to partially replace expensive stack testing commonly used in cold-start R&D.

The present paper is organized as follows. Section 2 presents a brief description of a non-isothermal cold start model built upon the work of Mao et al. [7], with particular focus on the key model elements describing coupled water and heat transport processes. Section 3 details an analysis of water flow, which holds a key to understanding and controlling PEFC cold start. In Section 4, comparisons of the results between non-isothermal and isothermal cold start are made in order to illustrate the profound effect of rising cell temperature. In addition, non-isothermal cold

* Corresponding author.
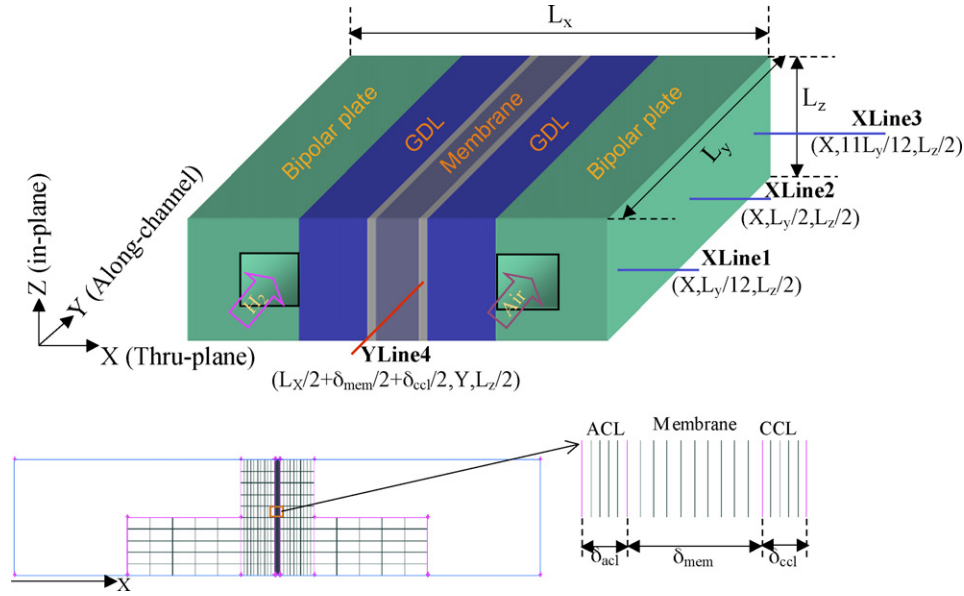*E-mail address:* cxw31@psu.edu (C.-Y. Wang).

Fig. 1. Geometry and meshing system of a single-channel PEFC. The four lines with coordinates indicated are chosen to display detailed numerical results.

start behaviors with different initial water content in the membrane/CL or from different startup temperatures are numerically explored. Finally, conclusions are summarized.

2. Non-isothermal cold-start model

We consider a PEFC consisting of nine sub-regions: two flow plates in anode and cathode, respectively, an anode channel, anode gas diffusion layer, anode catalyst layer, ionomeric membrane, cathode catalyst layer, cathode gas diffusion layer, and a cathode channel, as schematically shown in Fig. 1. Dry air and hydrogen are fed into the cathode and anode channels, respectively. A constant current density is applied to start up the cell from a sub-freezing temperature. We employ the multiphase model of Mao et al. [7] without introducing new physical processes other than treating the temperature as an evolving variable determined simultaneously from the energy equation. The 3D cold-start model of Mao et al. has been extensively validated against experimental data of product water, and thus is expected to be reliable for use to simulate isothermal cold start over a wide range of subzero temperatures. This model is briefly summarized here in the form of the following governing equations [7]:

Continuity equation

$$\frac{\partial(\varepsilon_s \rho_s)}{\partial t} + \frac{\partial(\varepsilon \rho)}{\partial t} + \nabla \cdot (\rho \vec{u}) = 0 \qquad (1)$$

Momentum conservation

$$\frac{\partial(\rho \vec{u}/\varepsilon)}{\partial t} + \nabla \cdot \left(\frac{\rho \vec{u} \vec{u}}{\varepsilon^2}\right) = \nabla \cdot (\mu \nabla \vec{u}) - \nabla P + S_u \qquad (2)$$

Energy conservation

$$\frac{\partial \left[(\rho c_p)_{\text{cell}} T\right]}{\partial t} + \nabla \cdot \left[\rho c_p \vec{u} T\right] = \nabla \cdot (k_{\text{eff}} \nabla T) + S_T \qquad (3)$$

Table 1
Geometrical parameters, operating conditions and material properties

Quantity	Value
Gas channel depth/width	1/1 mm
Land shoulder width	1 mm
Anode/cathode GDL thickness	300/300 μm
Anode/cathode CL thickness	10/10 μm
Membrane thickness	30 μm
Cell height/length	2/600 mm
Anode/cathode pressure	1.0 atm
Ambient startup temperature	253.15 K (default) or 263.15 K
Current density	100 mA/cm^2
Anode/cathode stoichiometry	2.0
Anode/cathode inlet gas temperature	Same as ambient temperature
Relative humidity of anode/cathode inlet gas	0.0%
Porosity of GDL	0.6
Porosity of CL	0.53
Volume fraction of ionomer in CL	0.15
Density of gas mixture	1.0 kg/m^3
Heat capacity of membrane/CL/GDL/bipolar plate	1650/3300/568/1580 kJ/m^3 K
Heat conductivity of membrane/CL/GDL/bipolar plate	0.95/1.0/1.0/20 W/m K
Heat capacity of ice/frost	3369.6 kJ/m^3 K
Heat conductivity of ice/frost	2.4 W/m K
Latent heat of desublimation	5.1 × 10^4 J/mol
Permeability of GDL/CL	1.0 × 10^{-12}/1.0 × 10^{-13} m^2
Electronic conductivity of GDL/CL/bipolar plate	300.0/300.0/1.0 × 10^7 S/m
Equivalent weight of ionomers	1.1 kg/mol
Density of dry membrane	1980 kg/m^3
H$_2$/H$_2$O diffusivity in anode	8.67 × 10^{-5}/8.67 × 10^{-5} m^2/s
O$_2$/H$_2$O diffusivity in cathode	1.53 × 10^{-5}/1.79 × 10^{-5} m^2/s

Table 2
Source terms for the conservation equations in each sub-region

	S_u	$S_C^{H_2O}$	S_C (for reactants)	S_{ϕ_s}	S_{ϕ_e}
Gas channels	0	0	0	0	–
Gas diffusion layers	$-\dfrac{\mu}{K_{GDL}}\vec{u}$	$-\dot{q}_{gs}^{H_2O}$	0	0	–
Catalyst layers	$-\dfrac{\mu}{K_{CL}}\vec{u}$	$-\nabla\cdot\left(\dfrac{n_d}{F}i_e\right)-\dfrac{s_k j}{nF}-\dot{q}_{gs}^{H_2O}$	$-\dfrac{s_k j}{nF}$	$-j$	j
Membrane	–	$-\nabla\cdot\left(\dfrac{n_d}{F}i_e\right)$	0	–	0

Note: Electrochemical reaction $\sum_k s_k M_k^z = ne^-$ where $\begin{cases} M_k \equiv \text{chemical formula of species } k \\ s_k \equiv \text{stoichiometry coefficient} \\ n \equiv \text{number of electrons transferred} \end{cases}$. In PEFC, there are (anode) $H_2-2H^+=2e^-$; (cathode) $2H_2O-O_2-4H^+=4e^-$.

Species conservation

$$\frac{\partial(\varepsilon C^i)}{\partial t} + \nabla\cdot(\vec{u}C^i) = \nabla\cdot(D_{eff}^i\nabla C^i) + S_C^i \quad (4)$$

Charge conservation (electrons)

$$0 = \nabla\cdot(\sigma_s^{eff}\nabla\phi_s) + S_{\phi_s} \quad (5)$$

Charge conservation (protons)

$$0 = \nabla\cdot(\kappa_e^{eff}\nabla\phi_e) + S_{\phi_e} \quad (6)$$

The porosity ε in the above equations becomes unity in the gas channel; while in porous layers it is not a constant as in normal operation but a variable depending on the intrinsic porosity ε_0 and the local ice fraction s, namely, $\varepsilon=\varepsilon_0(1-s)$. The volume fractions occupied by ice and by the solid matrix can be expressed as $\varepsilon_s=\varepsilon_0 s$ and $\varepsilon_m=1-\varepsilon_0$, respectively. Effective transport coefficients: D_{eff}, σ_s^{eff}, and κ_s^{eff} are modified by Bruggeman factor with an exponent of 1.5 to account for porosity and tortuosity effects. Geometrical parameters, operating conditions, and material properties are summarized in Table 1.

Source terms, S_u, S_c, S_{ϕ_s} and S_{ϕ_e}, in each sub-region are tabulated in Table 2. The fluid relative permeability K in porous layers is assumed to follow a cubic relation to the ice fraction s, i.e. $K=K_0(1-s)^3$. The major assumptions of the present model can be found in Mao et al. [7] and thus are not repeated here. However, key model elements related to the coupled water and heat transport processes, critical to describing non-isothermal cold start of main interest in this work, are elaborated below.

2.1. Water transport

Water transport through the membrane is of paramount importance during cold start. Here we consider electroosmotic drag and molecular diffusion while neglecting hydraulic permeation due to no liquid water present in the membrane at sub-freezing temperatures [11]. Dual mechanisms of water transport are numerically treated by a single-domain approach [12], namely, a generalized water transport equation valid in all regions of a cell is solved:

$$\frac{\partial(\varepsilon_{eff}C^{H_2O})}{\partial t} + \nabla\cdot(\vec{u}C^{H_2O}) = \nabla\cdot(D_{eff}^{H_2O}\nabla C^{H_2O}) + S_C^{H_2O} \quad (7)$$

where

$$\varepsilon_{eff} = \begin{cases} 1.0 & \text{in gas channels} \\ \varepsilon_0(1-s) & \text{in GDLs} \\ \varepsilon_0(1-s)+\varepsilon_{mem}\dfrac{1}{EW}\dfrac{RT}{p_{sat}}\left(\rho+\lambda\dfrac{d\rho}{d\lambda}\right)\dfrac{d\lambda}{da} & \text{in CLs} \\ \dfrac{1}{EW}\dfrac{RT}{p_{sat}}\left(\rho+\lambda\dfrac{d\rho}{d\lambda}\right)\dfrac{d\lambda}{da} & \text{in membrane} \end{cases} \quad (8)$$

and

$$D_{eff}^{H_2O} = \begin{cases} D_g^{H_2O} & \text{in gas channels} \\ [\varepsilon_0(1-s)]^{1.5}D_g^{H_2O} & \text{in GDLs} \\ [\varepsilon_0(1-s)]^{1.5}D_g^{H_2O}+\varepsilon_{mem}^{1.5}D_{mem}^{H_2O}\dfrac{1}{EW}\dfrac{RT}{p_{sat}}\left(\rho+\lambda\dfrac{d\rho}{d\lambda}\right)\dfrac{d\lambda}{da} & \text{in CLs} \\ D_{mem}^{H_2O}\dfrac{1}{EW}\dfrac{RT}{p_{sat}}\left(\rho+\lambda\dfrac{d\rho}{d\lambda}\right)\dfrac{d\lambda}{da} & \text{in membrane} \end{cases} \quad (9)$$

It is worth pointing out that due to absence of fluid flow (i.e. $\vec{u} = 0$) in the membrane, the second item in Eq. (7) naturally vanishes for water transport in the membrane. Both water diffusivities in gas and membrane phases, $D_{\mathrm{g}}^{\mathrm{H_2O}}$ and $D_{\mathrm{mem}}^{\mathrm{H_2O}}$, are strong functions of temperature T, namely

$$D_{\mathrm{g}}^{\mathrm{H_2O}} = D_0 \left(\frac{T}{353.15} \right)^{3/2} \left(\frac{P_0}{P} \right),$$

$$D_{\mathrm{mem}}^{\mathrm{H_2O}} = \begin{cases} 5.93 \times 10^{-5} \lambda \left(e^{0.28\lambda} - 1 \right) e^{(-4269/T)} & \text{for } 0 < \lambda \leq 3 \\ 7.97 \times 10^{-6} \lambda \left(1 + 161 \, e^{-\lambda} \right) e^{(-4269/T)} & \text{otherwise} \end{cases}$$

$$(10)$$

where the water diffusivity in the membrane follows the same dependence on water content as Motupally et al. [13], but for the dependence on temperature, the activation energy is modified following Mao et al. [7] due to different temperature ranges and membranes (i.e. Nafion for Motupally's correlation vs. Gore-Select membranes for Eq. (10)). These equations imply that water transport improves as the cell warms up during non-isothermal cold start, which in turn alters the characteristics of water flow and ice formation in CL. Hence, there is a major impact of rising cell temperature on cold-start performance.

2.2. Heat transport

During PEFC cold start, heat generation S_T in Eq. (3) can be determined by

$$S_T = \begin{cases} j \left(\eta + T \dfrac{dU_0}{dT} \right) + \dfrac{i_{\mathrm{e}}^2}{\kappa_{\mathrm{e}}^{\mathrm{eff}}} + \dfrac{i_{\mathrm{s}}^2}{\sigma_{\mathrm{s}}^{\mathrm{eff}}} + \dot{q}_{\mathrm{gs}}^{\mathrm{H_2O}} h_{\mathrm{gs}} & \text{in CLs} \\[2mm] \dfrac{i_{\mathrm{e}}^2}{\kappa_{\mathrm{e}}^{\mathrm{eff}}} & \text{in membrane} \\[2mm] \dfrac{i_{\mathrm{s}}^2}{\sigma_{\mathrm{s}}^{\mathrm{eff}}} + \dot{q}_{\mathrm{gs}}^{\mathrm{H_2O}} h_{\mathrm{gs}} & \text{in GDLs} \\[2mm] \dfrac{i_{\mathrm{s}}^2}{\sigma_{\mathrm{s}}^{\mathrm{eff}}} & \text{in bipolar plate} \end{cases}$$

$$(11)$$

Here, $j\eta$ and $jT(dU_0/dT)$ are irreversible reaction heat and entropic heat, respectively, which are generated from the oxygen reduction reaction; $i_{\mathrm{e}}^2/\kappa_{\mathrm{e}}^{\mathrm{eff}}$ and $i_{\mathrm{s}}^2/\sigma_{\mathrm{s}}^{\mathrm{eff}}$ stand for Joule heat arising from protonic and electronic resistances, respectively, and the last heat source, $\dot{q}_{\mathrm{gs}}^{\mathrm{H_2O}} h_{\mathrm{gs}}$, originates from latent heat of vapor desublimation into ice/frost at a sub-freezing temperature. This latent heat is directly proportional to the ice formation rate, $\dot{q}_{\mathrm{gs}}^{\mathrm{H_2O}}$, which is calculated under the assumption of instantaneous desublimation upon vapor saturation and numerically by following the large source term technique [14]. The membrane proton conductivity, which directly controls the Joule heat, is related to membrane water content by [7]

$$\kappa_{\mathrm{e}} = \exp \left[2222 \left(\frac{1}{303} - \frac{1}{T} \right) \right] (0.5139\lambda - 0.326)$$

$$(12)$$

Water transport, including ice growth/distribution, has tremendous impact on oxygen reduction reaction (ORR) kinetic overpotential and mass transport overpotential, which in turn dictate the reaction heat. In addition, thermophysical properties (i.e. thermal conductivity and heat capacity) present in the

energy conservation equation, Eq. (3), are also composition dependent, as expressed by the relevant formulas tabulated in Table 3. The vast majority of data in Table 3 is taken from Mao et al. [7].

The complete set of governing equations, Eqs. (1)–(6), contains nine unknowns: $\vec{u}$ (three components), P, T, $C^{\mathrm{H_2}}$ on the anode side or $C^{\mathrm{O_2}}$ on the cathode side, $C^{\mathrm{H_2O}}$ (or λ), ϕ_{e}, and ϕ_{s}. Appropriate boundary and initial conditions are required to close this mathematical system.

2.3. Boundary conditions

Zero-flux boundary conditions are prescribed at all external boundaries, except for the gas channel inlets and outlets, for flow, species transport, and heat transport equations. This means that thermally we are considering an adiabatic cell. Zero-flux boundary condition is also applied to the electrolyte phase potential, while for the electronic phase potential, a reference potential (zero) is set at the anode side and a constant flux (current density), $100 \, \mathrm{mA/cm^2}$, is prescribed at the outer surface of the cathode bipolar plate.

At the channel inlets, the gas velocity $\vec{u}_{\mathrm{in}}$ can be calculated from the stoichiometric flow ratio, i.e. ξ_{a} or ξ_{c}, defined at the current density, I, namely

$$\xi_{\mathrm{a}} = \frac{C^{\mathrm{H_2}} u_{\mathrm{in,a}} A_{\mathrm{in,a}}}{IA/2F}, \qquad \xi_{\mathrm{c}} = \frac{C^{\mathrm{O_2}} u_{\mathrm{in,c}} A_{\mathrm{in,c}}}{IA/4F}$$

$$(13)$$

The inlet gas temperature is set to be the initial startup temperature and the inlet species molar concentrations are calculated from the inlet pressure, temperature and humidity in terms of the ideal gas law. At the outlets, fully developed or zero-flux conditions are applied. The wall boundaries for gas flow are considered to be no-slip and impermeable.

2.4. Initial conditions

The initial temperature throughout the cell is set uniformly at the startup temperature. The reactant species in the gas channels and GDLs are initially set to have the same molar concentration as the inlet gas. At a sub-freezing temperature the residual water exists in the form of ice/frost. Pre-startup conditions, such as the initial ice fraction in CLs and initial water content in membrane and CL ionomers, are crucial to the fate of PEFC cold start. Gas purge is a popular procedure used to enhance PEFC cold-start performance. Bradean et al. [15] measured the MEA water content distribution after purge procedure and found that the initial ice/frost fraction in CLs/GDLs and the initial water content in membrane/CLs are dependent on the location along the flow direction (Y). Following the qualitative trend of data described by Bradean et al. [15], we assume the initial distribution of ice fraction in the CLs and GDLs as

$$s_0 = \begin{cases} 0 & \left(\dfrac{Y}{L_Y} < \dfrac{1}{6} \right) \\[2mm] 0.3 \left[1 - e^{-(Y-0.1)/0.05} \right] & \left(\dfrac{Y}{L_Y} \geq \dfrac{1}{6} \right) \end{cases}$$

$$(14)$$

Table 3
Electrochemical, physical and transport properties [7]

Description	Formulation/value
Anode transfer density, j (A/m^3)	$= (1-s)ai_{0,\mathrm{a}} \left(\dfrac{C_{H_2}}{C_{H_2,\mathrm{ref}}} \right)^{1/2} \left(\dfrac{\alpha_\mathrm{a}+\alpha_\mathrm{c}}{RT} F\eta \right)$
Cathode transfer density, j (A/m^3)	$= -(1-s)ai_{0,\mathrm{c}} \left(\dfrac{C_{O_2}}{C_{O_2,\mathrm{ref}}} \right) \exp\left(-\dfrac{\alpha_\mathrm{c}}{RT} F\eta \right)$
Surface overpotential, η (V)	$= \phi_\mathrm{s} - \phi_\mathrm{e} - U_0$
Anode/cathode equilibrium potential, U_0 (V)	$= 0/1.23 - 0.9 \times 10^{-3}(T - 298)$
Anode/cathode exchange current density × reaction surface area, $a_0 i_{0,\mathrm{a}}$ and $a_0 i_{0,\mathrm{c}}$ (A/m^3)	$= 10^9/10^4$
Anode/cathode transfer coefficient, α	$\alpha_\mathrm{a} + \alpha_\mathrm{c} = 2/\alpha_\mathrm{c} = 1$
Faraday constant, F (C/mol)	96487
Water saturation concentration, $C_{\mathrm{sat}}(T)$ (Pa)	$= \dfrac{p_{\mathrm{sat}}(T)}{RT}$, where $p_{\mathrm{sat}}(T) = 611.3 \exp\left[\dfrac{2.8345\times10^6}{R} \right] \left(\dfrac{1}{273.15} - \dfrac{1}{T} \right)$
Water content in membrane, λ	$= \begin{cases} 0.043 + 17.81a - 39.85a^2 + 36.0a^3 & \text{for } 0 < a \le 1 \\ 14 + 1.4(a-1) & \text{for } 1 < a \le 3 \end{cases}$
Ionic conductivity of membrane, κ_e (S/m)	$= \exp\left[2222 \left(\dfrac{1}{303} - \dfrac{1}{T} \right) \right] (0.5139\lambda - 0.326)$
H$_2$O diffusivity in membrane, $D_{\mathrm{mem}}^{H_2O}$ (m^2/s)	$D_{\mathrm{mem}}^{H_2O} = \begin{cases} 5.93 \times 10^{-5}\lambda(e^{0.28\lambda} - 1)e^{(-4269/T)} & \text{for } 0 < \lambda \le 3 \\ 7.97 \times 10^{-6}\lambda(1 + 161e^{-\lambda})e^{(-4269/T)} & \text{otherwise} \end{cases}$
Membrane density, ρ (kg/m^3)	$= \dfrac{1.98 + 0.0324\lambda}{1 + 0.0648\lambda} \times 10^3$
Gas diffusivity at non-standard condition, D (m^2/s)	$= D_0 \left(\dfrac{T}{353.15} \right)^{3/2} \left(\dfrac{P_0}{P} \right)$
EOD coefficient, n_d	$= f(\lambda, T) \approx 0 - 0.6$
Viscosity of anode and cathode gas, μ (Pa s)	$= 9.88 \times 10^{-6} X_{H_2} + 1.12 \times 10^{-5} X_{H_2O} + 2.01 \times 10^{-5} X_{N_2} + 2.3 \times 10^{-5} X_{O_2}$
Heat capacity of anode and cathode gas, ρc_p (J/m^3 K)	$= 1296.0 X_{H_2} + 1600.0 X_{H_2O} + 1249.2 X_{N_2} + 1283.8 X_{O_2}$
Heat conductivity of anode and cathode gas, k (W/m K)	$= 0.17 X_{H_2} + 0.024 X_{H_2O} + 0.024 X_{N_2} + 0.024 X_{O_2}$
Heat conductivity of anode and cathode gas, k (W/m K)	$= 0.17 X_{H_2} + 0.024 X_{H_2O} + 0.024 X_{N_2} + 0.024 X_{O_2}$
Heat capacity in porous layers, $(\rho c_p)_{\mathrm{cell}}$ (J/m^3 K)	$= \varepsilon_\mathrm{s}(\rho c_p)_\mathrm{s} + \varepsilon\rho c_p + \varepsilon_\mathrm{m}(\rho c_p)_\mathrm{m}$
Effective heat conductivity in porous layers, k_{eff} (W/m K)	$= \varepsilon_\mathrm{s} k_\mathrm{s} + \varepsilon k + \varepsilon_\mathrm{m} k_\mathrm{m}$

Similarly the initial distribution of water content in the membrane and CLs given below is used as the baseline.

$$\lambda_{0,1} = \begin{cases} 1.4 & \left(\dfrac{Y}{L_Y} < 1/6 \right) \\ 5.4 \left(\dfrac{Y}{L_Y} \right) + 0.5 & \left(1/6 \le \dfrac{Y}{L_Y} \le \dfrac{5}{6} \right) \\ 5.0 & \left(\dfrac{Y}{L_Y} > \dfrac{5}{6} \right) \end{cases} \qquad (15)$$

To study the effect of pre-startup conditions, a different initial water content distribution, $\lambda_{0,2}$, is also used. $\lambda_{0,2}$ has a similar profile as $\lambda_{0,1}$, while at the cell outlet portion $\lambda_{0,2}$ takes the saturated value (i.e. 14), much more humidified than the counterpart of $\lambda_{0,1}$. Fig. 2 displays the profiles of initial ice/frost distribution in the CLs/GDLs and initial water content in the membrane/CLs.
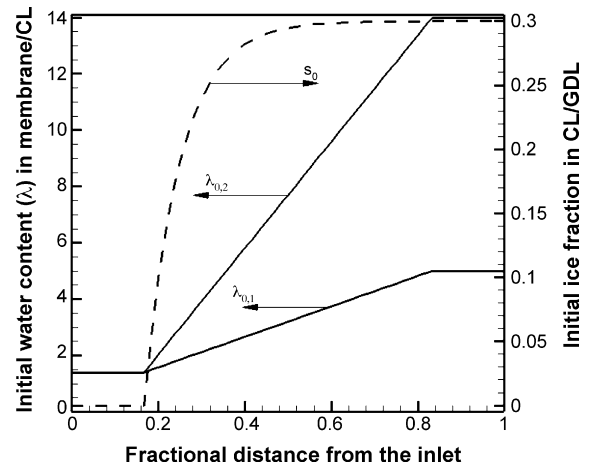

Fig. 2. Profiles of initial water content in the membrane/CL ionomers, and initial ice fraction in the CL pores.

2.5. Numerical procedures

The conservation equations together with the appropriate boundary/initial conditions are solved in the commercial CFD flow solver, Fluent® (version 6.2.16). By customizing its User Defined Functions (UDF), various source terms, physical properties, and non-standard advection–convective terms in the governing equations, Eqs. (1)–(6), are implemented. The well-known SIMPLE (semi-implicit method for pressure linked equation) algorithm is used to address the pressure–velocity coupling and the first order upwind differencing scheme is used for discretization of the velocity field. To accelerate convergence, the AMG (algebraic multi-grid) iterative method is applied to solve the linearized algebraic equations. Following the solution of flow field, the species, proton and electron phase potential equations are solved. Decoupling of the flow field from other equations, also called the constant flow assumption, has been carefully justified by Wang and Wang [16]. A fully implicit scheme is used to discretize the transient terms in order to maximize the time step and decrease the calculation time. The transient cold-start calculation is terminated once the cell voltage drops to 0.35 V or the maximum temperature inside the cell rises to $0\,^\circ C$ (followed by self-startup). The numerical mesh in the through-plane direction (X) is sketched in Fig. 1. The symmetry with respect to the middle X–Y plane (see Fig. 1) allows the numerical simulation to be carried out only in the upper-Z half of the single-channel fuel cell. The geometry and meshing system are based on the work by Mao et al. [7]. Results-independence studies with respect to mesh density and time step have been performed [17].

3. Analysis of water flow

As discussed in the previous work [3–9,17], water flow at a subzero temperature in the PEFC plays a central role in cold start. In the present work, water flow under non-isothermal conditions is of particular interest. Fig. 3 schematically shows water production and transport on the cathode side of a PEFC. ORR produces water in the cathode CL at a rate of $\dot{n}_{pro}$. Vapor-phase transport brings some water vapor into the cathode GDL and

Fig. 3. Schematic illustration of water flow during PEFC cold start. Redrawn after Mao and Wang [5].

gas channel. At the outlet of gas channels, some water emits to the ambient along with the exhaust gas ($\dot{n}_{outflow}$). Water on the anode side may be dragged to the cathode CL due to electroosmotic drag (EOD). At the interface of the cathode CL and membrane, water diffuses into the membrane via back diffusion. Excess water accumulating in the cathode CL and GDL will desublimate into ice/frost once the local water vapor becomes oversaturated. Letting $\dot{n}_{CCL}$, $\dot{n}_{mem}$, $\dot{n}_{anode}$, and $\dot{n}_{ice}$ represent the water uptake rate in the ionomer of cathode CL, water uptake rate in the membrane, water transport rate from the anode side, and ice formation rate in the cathode CL/GDL, respectively, an overall water balance can be written as

$$\dot{n}_{pro} + \dot{n}_{CCL} + \dot{n}_{mem} + \dot{n}_{anode} + \dot{n}_{ice} + \dot{n}_{outflow} = 0 \qquad (16)$$

where $\dot{n}_{pro}$ is designated with a positive sign; then $\dot{n}_{CCL}$, $\dot{n}_{ice}$, and $\dot{n}_{outflow}$ are always negative as they take away the product water. In the membrane (or anode), if water back diffusion dominates the water content variation, $\dot{n}_{mem}$ (or $\dot{n}_{anode}$) takes a negative value, otherwise a positive value.

Mathematically all the quantities in Eq. (16) can be determined by

$$\dot{n}_{pro} = \frac{M^{H_2O}}{A} \int_{V,CCL} -\frac{j}{2F}\,dV,$$

$$\dot{n}_{CCL} = -\frac{M^{H_2O}}{A} \frac{\rho\varepsilon_{mem}/EW \int_{V,CCL}(\lambda|_{t+\Delta t}-\lambda|_t)\,dV}{\Delta t},$$

$$\dot{n}_{mem} = -\frac{M^{H_2O}}{A} \frac{\rho/EW \int_{V,mem}(\lambda|_{t+\Delta t}-\lambda|_t)\,dV}{\Delta t},$$

$$\dot{n}_{anode} = -\frac{M^{H_2O}}{A} \frac{\rho\varepsilon_{mem}/EW \int_{V,ACL}(\lambda|_{t+\Delta t}-\lambda|_t)\,dV}{\Delta t},$$

$$\dot{n}_{ice} = -\frac{M^{H_2O}}{A} \int_{V,CCL\,and\,CGDL} \dot{q}_{gs}^{H_2O}\,dV,$$

$$\dot{n}_{outflow} = -\frac{M^{H_2O}}{A} \int_{A,outlets} C^{H_2O} u_{out}\,dA \qquad (17)$$

Note that all the rate quantities are multiplied by a factor of M^{H_2O}/A so as to have a unit of $kg/m^2\,s$.

4. Results and discussion

It should be pointed out that extensive validation of the present cold-start model against experimental data under isothermal conditions has been carried out by Mao et al. [7] and Mao [17] with $\pm 20\%$ accuracy. The validation therefore establishes the validity of basic physics underlying PEFC cold start, as contained in the present model.

A set of simulations has been performed to understand the physics of coupled water and heat transport involved in non-isothermal PEFC cold start. The startup current density is fixed at $100\,mA/cm^2$. Four representative lines, XLine1, XLine2, XLine3 and YLine4 with coordinates explicitly marked in Fig. 1, are chosen for the presentation of detailed numerical results.
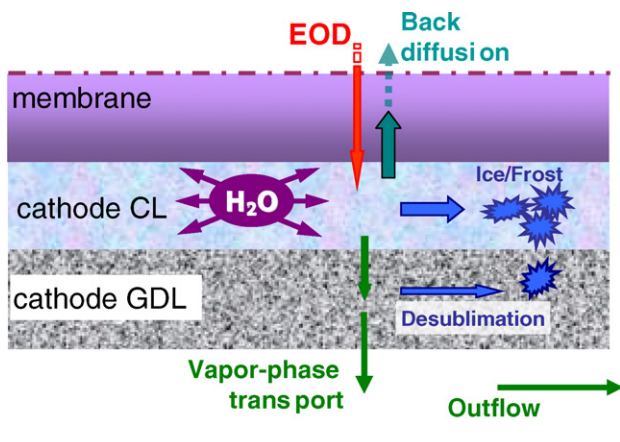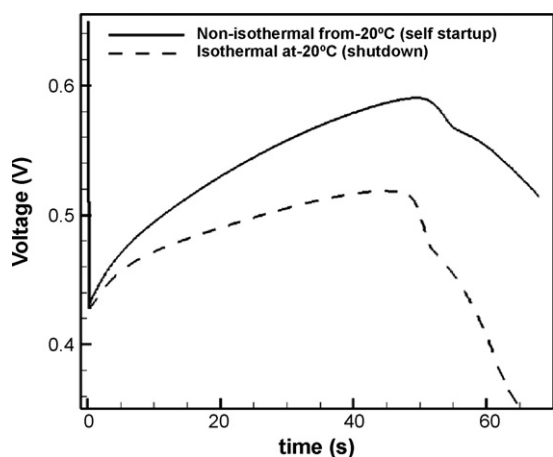
Fig. 4. Comparison of cell voltage curves in non-isothermal cold start from −20 °C and isothermal cold start at −20 °C.

Fig. 5. Water content profiles in MEA in the through-plane direction (along XLine2) during non-isothermal cold start from −20 °C and isothermal cold start at −20 °C.

4.1. Effect of rising cell temperature

Two sets of results, one for non-isothermal cold start from −20 °C and the other for isothermal cold start at −20 °C under otherwise identical conditions, are compared here to demonstrate the effect of rising cell temperature on cold start. Isothermal cold-start simulation was realized by fixing the cell temperature at the initial startup temperature; thus the solution does not include the energy conservation equation, Eq. (3). Since no temperature evolution occurs under the isothermal situation, any difference observed between the results of the non-isothermal and isothermal simulations can be attributed to the rising cell temperature effect.

Fig. 4 plots cell voltage curves for these two cases. Initial water content in the membrane and CLs is $\lambda_{0,1}$, i.e. the membrane is relatively dry. Thus, the protonic resistance is very high and the cell voltage instantaneously drops down to 0.43 V upon load. Subsequently, the cell voltage is seen to increase as water produced from ORR gradually hydrates the membrane and ionomer in the CLs, leading to a lowering of protonic resistance. Once water vapor concentration inside the cathode CL reaches saturation, ice begins to form. Ice formed blocks the pathways for oxygen transport and reduces electrochemical active area (ECA), leading to larger voltage loss; consequently, at ∼48 s into startup, the cell voltage begins to drop. When the ice fraction in cathode CL approaches unity, cell operation quickly shuts down as can be seen in the isothermal case. In a cell with non-uniform initial distribution of water, the shutdown may occur in a cascade fashion. Towards the cell outlet, the one sixth of the cell where the initial water content in the membrane/CLs is uniformly highest (see Fig. 2), the rate of ORR is highest, resulting in earliest shutdown of this portion of the cell. Then the shutdown gradually extends to the other parts of the cell. This cascading shutdown process can be observed from distinctly different slopes of the cell voltage curve during voltage dropdown.

The membrane water diffusivity is a strong function of cell temperature, as expressed in Eq. (10). The rising cell temperature during non-isothermal cold start gives rise to higher membrane water diffusivity and more water diffused into the membrane.
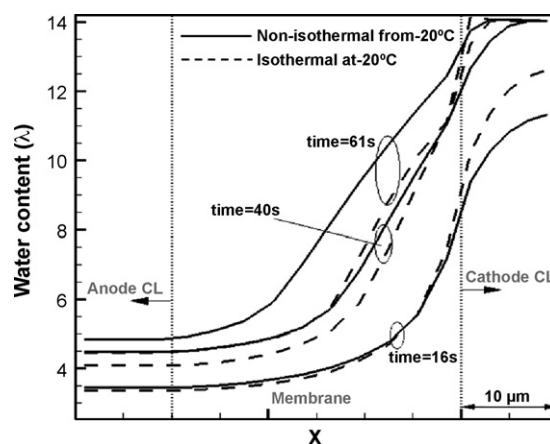
The more hydrated membrane and the rising cell temperature, in turn, result in lower protonic resistance during non-isothermal cold start. Therefore, as seen from Fig. 4, the cell voltage during non-isothermal cold start remains higher than the isothermal case and the difference between the two enlarges with time.

At ∼65 s into startup, the cell voltage of the isothermal cold start drops down to 0.35 V, with almost half of the cell being shut down. In contrast, at 67 s into non-isothermal cold start, the maximum temperature inside the cell reaches the freezing point, meaning that ice begins to melt and the cell voltage will recover subsequently. This is therefore a successful self-startup. More discussion on the temperature evolution during non-isothermal cold start is presented shortly in relation to Fig. 9.

Fig. 5 displays the water content profiles in MEA in the through-plane direction, along XLine2 located at the middle of the cell (see Fig. 1). Overall, there is higher water content in the membrane during non-isothermal cold start than in the isothermal case, indicating much more water stored in the membrane and hence less ice formation in the catalyst layer during non-isothermal cold start. The rising cell temperature in the non-isothermal cold start facilitates water diffusion from the cathode CL into the membrane and hence diverts ice formation in the cathode CL. This is a primary reason for substantially improved cold-start performance under non-isothermal conditions.

The ice fraction profiles at the center of cathode CL along the flow direction, YLine4 (see Fig. 1), are shown in Fig. 6. Because the initial water content in the membrane and CLs is highest towards the cell outlet (see Fig. 2), more ice forms in this region and then gradually extends to the other parts. Generally, the isothermal cold start yields more ice formation and hence lower cold-start performance. At 61 s, the cell outlet portion is full of ice for both non-isothermal and isothermal cold start, signifying this part of the cell being shut down. The current load is then redistributed to regions unplugged or partially plugged by ice with higher local current densities in order to compensate for shutdown area. The shutdown will quickly spread to the whole cell leading to a cascading failure. Indeed, this is the event experienced in isothermal cold start. However, in the non-isothermal cold start, the local temperature in some parts of the
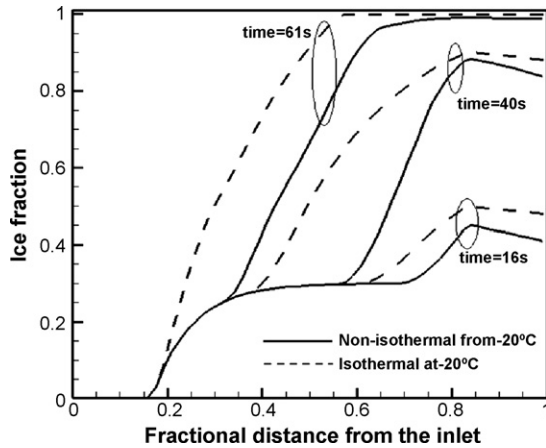
Fig. 6. Ice fraction profiles along flow direction at the center of cathode CL (along YLine4) during non-isothermal cold start from −20 °C and isothermal cold start at −20 °C.

Fig. 8. Evolution of various heat generation during non-isothermal cold start from −20 °C.

cell has already risen to the freezing point at ∼67 s, followed by ice melting and continuous operation of the startup.

As analyzed in the preceding section, Fig. 7 compares water flow between the two cold-start processes. The calculated water production rate is seen to be ∼0.0093 mg/cm² s, in exact agreement with that estimated from $M^{H_2O}I/2F$ with the current density of $I = 100$ mA/cm². Fig. 7 also shows that the primary mechanism for removing product water is via diffusion into the membrane, with the water removal via outflow being negligible as expected for very low temperatures (i.e. very low vapor saturation pressures). The water uptake in the ionomer of cathode CL is initially significant as the ionomers are initially dry prior to cold start, but this amount of water storage diminishes after ∼25–30 s. The balance of water between produced and transported forms ice in the cathode CL. It can be clearly seen that there is less ice formation in the non-isothermal case (Fig. 7a) than the isothermal (Fig. 7b), due primarily to the differing rate of membrane water uptake. Rising cell temperature in the non-isothermal cold start promotes membrane water uptake and slows down ice formation. More specifically, when ice begins to form (at ∼5 s), water content in the CL is highest (in saturation with ice precipitation) whereas water content in the membrane remains lowest at the initial value. This sets up the greatest concentration gradient to drive the highest water flux into the membrane, as can be seen
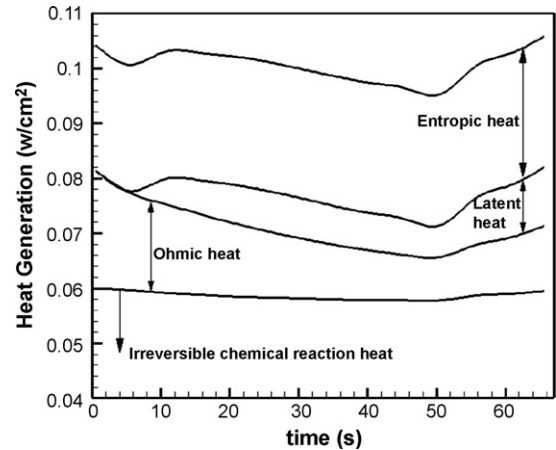
from Fig. 7. After this peak, the membrane water flux decreases under the isothermal condition due to diminishing water concentration gradient as the membrane gradually absorbs water (see Fig. 7b). However, under the non-isothermal condition, the membrane water flux remains high due to the rising cell temperature or enhanced water diffusivity in spite of the diminishing water concentration gradient (see Fig. 7a).

As indicated above, cell temperature rise plays a pivotal role in avoiding ice formation in the cathode CL and hence improving the cold-start performance. The temperature rise depends primarily on heat generation and transport in a PEFC, besides the thermal mass of the cell. Heat generation consists of four components: entropic heat, irreversible reaction heat, Ohmic heat, and latent heat due to the formation of ice/frost. Integrated over the entire cell, various heat generation rates are shown as function of time in Fig. 8. Overall, the entropic heat, irreversible reaction heat, Ohmic heat, and latent heat contribute to ∼23, 56, 8–20 and 0–12% of the total heat generation, respectively. The irreversible reaction heat and reversible entropic heat, dominating the cell temperature evolution, are associated with ORR and vary only slightly throughout the cold-start process. The Ohmic heat decreases at the early stage owing to membrane water uptake and resistance reduction. However, after ∼50 s, partial shutdown of the cell occurs and the Ohmic heat increases subsequently. The
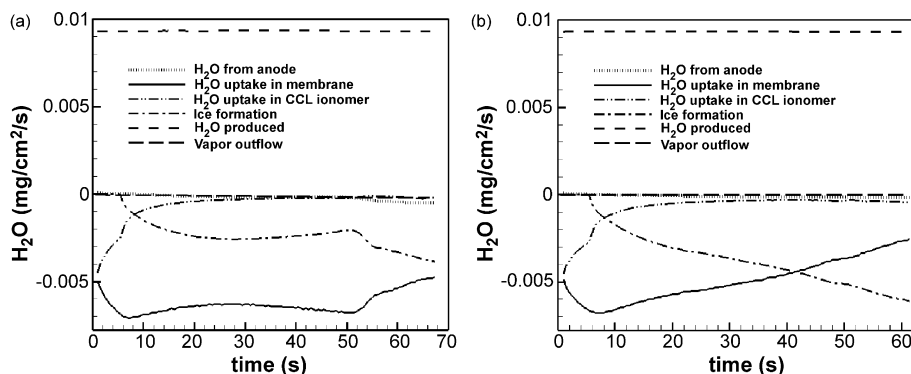

Fig. 7. Comparison of water flow in: (a) non-isothermal cold start from −20 °C, and (b) isothermal cold start at −20 °C.
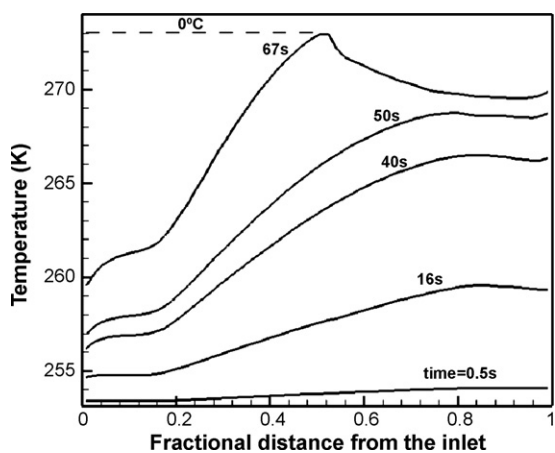
Fig. 9. Temperature profiles at the center of cathode CL (along YLine4) during non-isothermal cold start from −20 °C.

latent heat is dependent on the ice formation rate. Ice does not form until ∼5 s into cold start. Hence, the latent heat is zero at the beginning and remains almost constant within 10–50 s, after which it increases due to partial shutdown of the cell and substantially more ice formation.

The temperature profiles along the flow (along YLine4) during non-isothermal cold start are plotted in Fig. 9. With cell operation at 100 mA/cm^2, heat generation warms up the cell, and the highest local temperature always corresponds to the position where the rate of ORR is highest. Prior to 50 s into the cold start, the cell outlet region produces the highest ORR reaction current due to the highest membrane water content initially. Consequently, a temperature peak appears towards the cell outlet. At ∼61 s, the cell outlet portion fills with ice (see Fig. 6), which forces the highest reaction current to shift toward the middle of the cell. Hence, at 67 s, the highest temperature appears at a central position, as shown in Fig. 9. Note that the maximum temperature inside the cell has reached the freezing point at 67 s, indicative of a successful self-startup.

Fig. 9 clearly indicates a strong non-uniformity in temperature distribution during cold start. That is, at 67 s some portion of the cell already breaks through the freezing point while the average cell temperature is still much below the freezing. On the other hand, one can simply estimate the average cell temperature using a lumped thermal analysis for the entire cell. One can sum up the total heat generated and the cell thermal mass of all components including the membrane, CLs, GDLs and bipolar plates according to the geometrical dimensions tabulated in Table 1. Assuming that the cell is well insulated and heat loss to the exhaust gas is negligible, it follows that it requires approximately 102.7 s to warm up the cell from −20 to 0 °C. The lumped thermal model over-estimates the heat required of self-startup by ∼50% and apparently cannot fully delineate the localized interactions between heat and water transport during non-isothermal cold start. This can be easily explained by the fact that PEFC subzero startup requires only a portion of its active area to reach the freezing point and stay ice-free and operable.

4.2. Effect of pre-startup condition

Pre-startup condition, i.e. initial water content in the membrane and CLs, is crucial to cold start. We compare two non-isothermal simulations: one with the initial water content profile $\lambda_{0,1}$ in the membrane and CLs, the other with $\lambda_{0,2}$. Both profiles are displayed in Fig. 2. The $\lambda_{0,2}$ profile represents an initially wetter membrane, especially towards the outlet. This case mimics ineffective gas purge prior to cold start, while the $\lambda_{0,1}$ profile can be regarded as result from effective gas purge.

Fig. 10 compares the cell voltage evolutions for these two cold-start operations with differing initial water content distributions. In contrast to the cold start with initial water content $\lambda_{0,1}$, the cell voltage does not feature a rise period due to initial membrane resistance improvement, but drops continually as a result of ice formation. At ∼25 s, the cell voltage drops down to 0.35 V, and almost half of the cell is shut down by ice filling. The drastically different fate of the two cold-start operations demonstrates the paramount importance of gas purge in creating favorable residual water distribution for cold start.

Figure 11 compares the water content profiles in MEA in the through-plane direction during these two cold-start operations. The profiles are shown along three representative lines: XLine1, XLine2 and XLine3, which denote the inlet, middle and outlet of the cell, respectively (see Fig. 1). In the case with initial water content $\lambda_{0,1}$ (Fig. 11a), water content in both the membrane and anode CL increases with time, indicating that back diffusion dominates and water is absorbed in the membrane. However, for the non-isothermal startup with initial water content $\lambda_{0,2}$ (Fig. 11b), at the cell outlet portion, due to the initially fully-hydrated membrane, the water concentration gradient (driving force of back diffusion) does not exist and EOD controls the water transport, resulting in water loss with time from the anode CL and membrane. At the middle of the cell, the combined effect of back diffusion and EOD increases the membrane water content next to the cathode CL but decreases water content neighboring the anode CL. At the cell inlet portion, the membrane is initially quite dry; thus back diffusion is strong and dominates water absorption in the membrane.
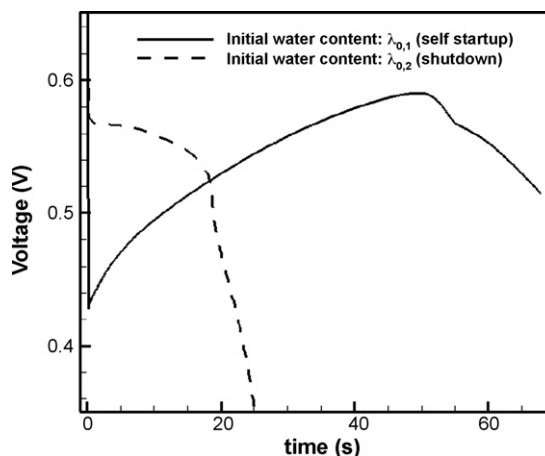

Fig. 10. Cell voltage evolutions for non-isothermal cold-start processes (from −20 °C) of different initial water content in the membrane/CL.
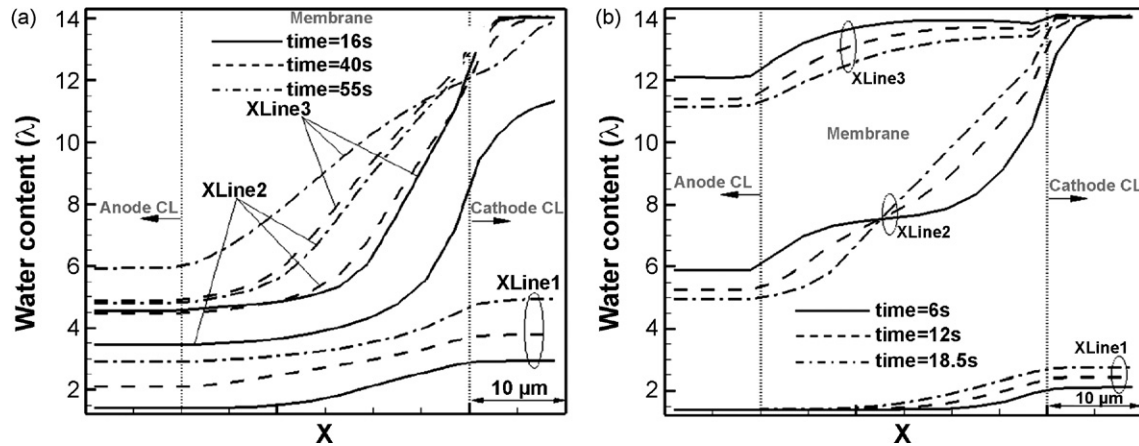
Fig. 11. Water content profiles in MEA along the through-plane direction in non-isothermal cold start from $-20\,^\circ$C with initial water content of: (a) $\lambda_{0,1}$, and (b) $\lambda_{0,2}$ in the membrane/CL.

A water flow chart for the non-isothermal cold start with initial water content $\lambda_{0,2}$ is displayed in Fig. 12. Due to the high initial water content towards the cell outlet (see Fig. 2), the MEA there has limited water storage potential. Overall, the membrane cannot uptake much water from the cathode CL. As shown from Fig. 12, water absorption in the membrane is quite small and occurs only at the beginning of startup; at the later stages the membrane even releases some water due to EOD. This is the chief difference between the two cases with differing initial water content profiles. The other striking difference is the fact that EOD also drags some water from the anode into the cathode CL for ice formation, as shown in Fig. 12. As a result, ice formation in the case with $\lambda_{0,2}$ profile is much faster and even exceeds the water production rate within about 14–18 s, eventually shutting down the entire cathode CL at 25 s. Because a successful self-startup requires the cell temperature to be elevated to $0\,^\circ$C before the cathode CL is completely filled by ice, sufficient water storage in the membrane is essential.
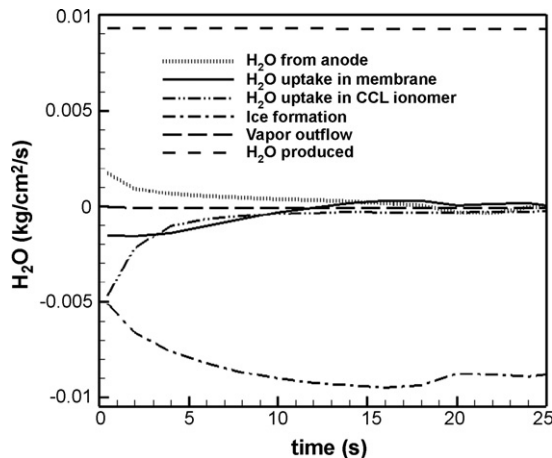
4.3. Effect of startup temperature

Finally, the effect of the ambient startup temperature is explored by performing a non-isothermal cold-start simulation from $-10\,^\circ$C. Fig. 13 compares the cell voltage curves for non-isothermal cold start from -10 and $-20\,^\circ$C. The higher startup temperature improves the membrane proton conductivity; thus the cell voltage upon current loading starts from a higher value, $\sim$0.5 V in comparison to 0.43 V in the case of $-20\,^\circ$C startup. At $\sim$34 s into $-10\,^\circ$C startup, the maximum temperature inside the cell already reaches $0\,^\circ$C, signifying a fast self-startup. Two reasons contribute to this fast self-startup. One is that the energy required to bring the cell temperature to $0\,^\circ$C is approximately half of that for $-20\,^\circ$C startup. The second is that a large fraction of the water produced from ORR is stored in the membrane as the water diffusivity in the membrane is significantly enhanced and consequently ice formation in the cathode CL diminishes. Indeed, the lack of voltage dropdown before the cell temperature rises from -10 to $0\,^\circ$C, as shown in Fig. 13, is indicative of virtually no ice formation in the cathode CL.

Fig. 12. Water flow in non-isothermal cold start (from $-20\,^\circ$C) of initial water content $\lambda_{0,2}$ in the membrane/CL.
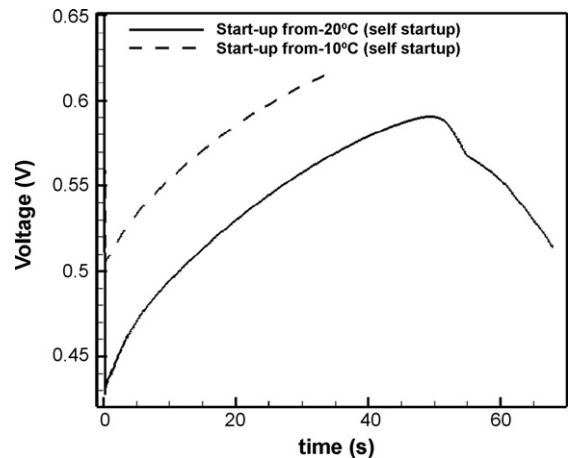

Fig. 13. Cell voltage evolutions for non-isothermal cold-start processes of different startup temperatures.
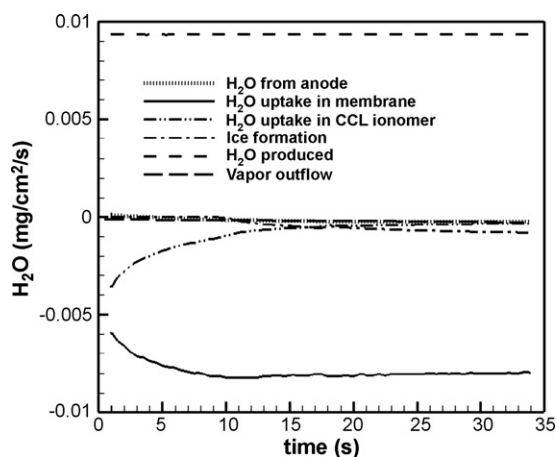
Fig. 14. Water flow in non-isothermal cold start from $-10\,^\circ$C.

Fig. 14 presents the water flow charts during non-isothermal cold start from $-10\,^\circ$C. The high startup temperature promotes membrane water uptake. Comparing Fig. 14 with Fig. 7a ($-20\,^\circ$C startup), it is found that almost all the product water is absorbed by the membrane in the $-10\,^\circ$C startup, leaving little water for ice formation in the cathode CL. Therefore, cold start is much easier from higher ambient startup temperatures.

5. Conclusions

During PEFC cold start, product water can be removed via diffusion into an initially dry membrane and vapor-phase transport into a GDL, thereby reducing ice formation in the cathode CL and the possibility of cell shutdown. Both mechanisms of water removal hinge strongly upon the cell temperature. Therefore, the rising cell temperature during non-isothermal cold start interacts non-linearly with water transport, creating a complex scenario for PEFC cold start. The fate of a subzero startup, whether shutdown or self-start, is ultimately determined by the competition between heat generation and ice formation in the catalyst layer. Generally, factors that promote cell warm-up and demote ice formation in the cathode CL have positive impact on PEFC cold start. Some obvious examples are low thermal mass of a stack, effective gas purge to minimize residual water in the stack prior to cold start, and higher ambient startup temperatures. Less obvious but useful examples are small improvements in MEA properties and/or operating parameters that lead to delayed ice formation in the CL, which then offers more time for heat generation and cell warm-up. Higher cell temperatures in turn delay ice formation in the CL. This non-linear feedback can eventually lead to successful self-start. The main utility of the present model is to provide a tool to delineate such intricate interactions between heat generation and ice formation and hence a design tool for the development of self-startup strategies.

More specifically, the effect of rising cell temperature on PEFC cold start is elaborated by comparing a non-isothermal cold start with an isothermal one. It is found that more water is transported into the membrane and less ice formation occurs in the cathode CL in the presence of rising cell temperature. In addition, the more hydrated membrane and the rising cell temperature greatly lower the membrane resistance, resulting in higher cell voltage. A lumped stack thermal model cannot adequately describe the thermal requirement of PEFC cold start, since the reaction current and heat generation are highly location dependent and cold start needs only a portion of the active area to be ice-free and operable.

It is also found that pre-startup conditions have significant influence on cold start. Procedures performed to minimize residual water inside the cell prior to cold start, such as gas purge, are critically important. Finally, non-isothermal cold start becomes much easier at higher ambient temperatures, as expected.

Appendix A

a	water activity or effective catalyst area per unit volume (m^{-1})
A	area; electrode area (m^2)
C	species concentration (mol/m^3)
D	species diffusivity (m^2/s)
EW	equivalent weight of dry membrane (kg/mol)
h	latent heat of vapor desublimation (J/mol)
i	superficial current density (A/m^2)
I	current density (A/m^2)
j	transfer current density (A/m^3)
k	heat conductivity (W/m K)
K	permeability (m^2)
M	molar mass (kg/mol)
n_d	electroosmotic drag coefficient (H$_2$O/H$^+$)
P	pressure (Pa)
$\dot{q}$	water desublimation rate (mol/m^3 s)
R	universal gas constant (8.314 J/mol K)
s	ice fraction defined as the ratio of ice volume to pore volume
S	source/sink
t	time (s)
Δt	time interval (s)
T	temperature (K)
u	superficial gas velocity (m/s)
U_0	equilibrium potential (V)
U_{cell}	cell voltage (V)
X	molar fraction

Greek symbols

ε	porosity or volume fraction
ϕ	phase potential (V)
η	surface overpotential (V)
κ	proton conductivity (S/m)
λ	water content (mol H$_2$O/mol SO$_3^-$)

μ	viscosity (Pa s)
ρ	density (kg/m^3)
σ	electronic conductivity (S/m)
ξ	stoichiometric flow ratio

Subscripts/superscripts

a/c	anode/cathode
C	species
e	electrolyte
eff	effective
g	gas
gs	vapor-solid phase transition
i	species or component
in/out	channel inlet/outlet
m	porous matrix
mem	membrane
ref	reference
s	ice or solid phase
sat	saturated
T	heat
u	momentum
0	initial, intrinsic or standard
ϕ_e/ϕ_s	electrolyte/electron potential
$-$	average
$\rightarrow$	vector

References

[1] Y. Hishinuma, T. Chikashisa, F. Kagami, T. Ogawa, JSME Int. J. B 47 (2004) 235.
[2] M. Oszcipok, D. Riemann, U. Kronenwett, M. Kreideweis, M. Zedda, J. Power Sources 145 (2005) 407.
[3] L. Mao, K. Tajiri, S. Ge, X.G. Yang, C.Y. Wang, 208th Electrochemical Society Meeting, Los Angeles, CA, October 16–21, 2005 (Abstract #998).
[4] S. Ge, C.Y. Wang, Electrochem. Solid-State Lett. 9 (2006) A499.
[5] L. Mao, C.Y. Wang, J. Electrochem. Soc. 154 (2007) B139.
[6] K. Tajiri, Y. Tabuchi, C.Y. Wang, J. Electrochem. Soc. 154 (2007) B147.
[7] L. Mao, C.Y. Wang, Y. Tabuchi, J. Electrochem. Soc. 154 (2007) B341.
[8] K. Tajiri, Y. Tabuchi, F. Kagami, S. Takahashi, K. Yoshizawa, C.Y. Wang, J. Power Sources 165 (2007) 179.
[9] S. Ge, C.Y. Wang, Electrochim. Acta 52 (2007) 4825.
[10] J. Hou, H. Yu, B. Yi, Y. Xiao, H. Wang, S. Sun, P. Ming, Electrochem. Solid-State Lett. 10 (2007) B11.
[11] G. Luo, H. Ju, C.Y. Wang, J. Electrochem. Soc. 154 (2007) B316.
[12] C.Y. Wang, Chem. Rev. 104 (2004) 4727.
[13] S. Motupally, A.J. Becker, J.W. Weidner, J. Electrochem. Soc. 147 (2000) 3171.
[14] V.R. Voller, Numer. Heat Trans. B 17 (1990) 155.
[15] R. Bradean, H. Haas, A. Desousa, R. Rahmani, K. Fong, K. Eggen, D. Ayotte, A. Huang, 2005 ACS Annual Meeting-Fuel Processing Session I: Modeling and System Integration, Cincinnati, OH, October 30–November 4, 2005.
[16] Y. Wang, C.Y. Wang, J. Electrochem. Soc. 152 (2005) A445.
[17] L. Mao, Ph.D. Thesis, The Pennsylvania State University, University Park, Pennsylvania, 2006.